Nanostructures for Solar Energy Harvesting

Mariana Sofia Santos
mariana.sofia.santos@tecnico.ulisboa.pt

***Abstract*—Renewable energy sources are more and more essential to energy production as the society evolves towards a fossil fuel free world. Solar energy is one of the most abundant sources of green energy. Nanoantennas can be used to improve and enhance the absorption of light into a PV cell in order to generate more current. In this study different nanoantennas structures are analyzed in tandem with a Silicon solar cell, as an effort to improve its output. The nanoantennas studied are metallic aperture nanoantennas made up of either Silver, Aluminium, Gold or Copper. The three geometries compared were rectangular, circular and triangular. The maximum field enhancement obtained was for an Aluminium rectangular nanoantenna of 50 nm thickness. Despite this, the geometry with more improvements compared with a Silicon basic cell was the circle geometry with a 100 nm radius.**

***Index Terms*—Electric Field Concentration, Nanoantennas, Optoelectronic devices, Photovoltaic Technology, Solar Energy Harvesting, Surface Plasmon Polaritons**

I. Introduction

The global population is estimated to reach 9.7 billion by 2050. With the growth of society comes the inherent increase of energy demand. The current production of energy relies heavily on fossil fuels which have an undesirable environmental impact. This aligned with the energy crisis, in which the prices of fossil fuels keep rising, for example, in September 2021 the price of natural gas was as high as 6.5 times the price of 2019.

Alternatively, photovoltaic cells convert solar power into DC electric power at a somewhat low price, and in a more environmental friendly way. In addition, PV cells require very little maintenance and are robust devices, which makes them attractive in the global energy market. In particular, the solar energy global market was valued at $52.5 billion in 2018 and is projected to reach $223.3 billion by 2026.

The solar radiation that reaches the earth in one day is enough to mitigate the earth's total energy needs for a year. However, in PV cells the efficiency is limited by the bandgap of the material. Each photon with energy above the bandgap produces an electron-hole pair independently of its energy. Photons that have an energy matched to the bandgap will produce the same energy delivered from high energy photons. This limits the efficiency to approximately 30% for single junction cells, and around 55% for multi-junction cells.

The idea of using nanoantennas as an alternative to solar cells was first proposed by Bailey in 1972. The use of nanoantennas in photovoltaics has gained a significant amount of interest in the last few years, considering they are expected to be more efficient and inexpensive. In addition, solar nanorectennas are not only expected to exceed PV devices efficiency during the day, but also by their ability to function during the night, making them less susceptible to weather conditions.

In more recent studies there has been an effort to combine the conventional PV with nanoantennas. This has been done either by laying the nanoantenna on top of the PV cell or in between layers of the PV cell, as an effort to increase light trapping.

II. State of Art

A. Optical Properties of Metals

It is particularly important to characterize the metals' optical behaviour since optical antennas rely on the resonance and plasmonic characteristics of the metals as a way to enhance radiation. The dielectric permittivity is the physical quantity that describes the metal's behaviour under an external electric field.

The Drude-Lorentz model describes the metals' properties at optical wavelengths by a complex dielectric function. In 1900, Paul Drude depicted the behaviour of the metals' electrons as those of an ideal gas, hence the Drude model, also known as the free-electron model. Later, this model proved incomplete as it only describes the intraband electron transitions or the free-electron effects, conveying metals' behaviour at infrared wavelengths and higher, presented on equation 1 [1]–[3].

$$\overline{\varepsilon}_{Drude}(\omega) = 1 - \frac{\Omega_p^2}{\omega(\omega + j\Gamma_0)} \tag{1}$$

Subsequently, to characterize the interband electron transitions(or bound-electron effects), an equivalent to the Lorentz insulators' model is added to the complex dielectric function, represented by equation 2.

$$\overline{\varepsilon}_{bound}(\omega) = \sum_{n=1}^{N} \frac{f_n \omega_p^2}{(\omega_n^2 - \omega^2) - j\omega\Gamma_n} \tag{2}$$

Thus, expanding the model to near-infrared and visible wavelength region. The Drude-Lorentz model describes the frequency dependence of the metal's permittivity, relating the dielectric function with the incident wave wavelength through equation 3. In this equation, ω_p is the metal's plasma frequency, N is the number of resonances with resonance frequency ω_n, with a certain oscillator's strength f_n and damping coefficient Γ_n. The Ω_p is the plasma frequency related with intraband transitions given by $\Omega_p = \sqrt{f_0}\omega_p$, with oscillator strength f_0 and damping coefficient Γ_0 [1]–[3].

$$\overline{\varepsilon}_{DL}(\omega) = 1 - \frac{\Omega_p^2}{\omega(\omega + j\Gamma_0)} + \sum_{n=1}^{N} \frac{f_n \omega_p^2}{(\omega_n^2 - \omega^2) - j\omega\Gamma_n} \tag{3}$$

In 1998, Rakic et al. conducted a fitting of the Drude Lorentz model parameters for several metals. However, this study focuses on four metals, silver (Ag), aluminium (Al), gold (Au) and copper (Cu), for which table I contains the parameters previously mentioned [4].

TABLE I: Drude-Lorentz parameters.

Parameters	Ag	Al	Au	Cu	
$\hbar\omega_p$	9.01	14.98	9.03	10.83	eV
f_0	0.845	0.523	0.760	0.575	
Γ_0	0.048	0.047	0.053	0.03	eV
f_1	0.065	0.227	0.024	0.061	
Γ_1	3.886	0.330	0.241	0.378	eV
ω_1	0.816	0.162	0.415	0.291	eV
f_2	0.124	0.050	0.010	0.104	
Γ_2	0.452	0.312	0.345	1.056	eV
ω_2	4.481	1.544	0.830	2.957	eV
f_3	0.011	0.166	0.071	0.723	
Γ_3	0.065	1.351	0.870	3.213	eV
ω_3	8.185	1.808	2.969	5.3	eV
f_4	0.840	0.030	0.601	0.638	
Γ_4	0.916	3.382	2.494	4.305	eV
ω_4	9.083	3.473	4.304	11.18	eV
f_5	5.646	-	4.384	-	
Γ_5	2.419	-	2.214	-	eV
ω_5	20.29	-	13.32	-	eV

Through equation 3, it was possible to obtain the following curves for the studied metals' complex dielectric function.

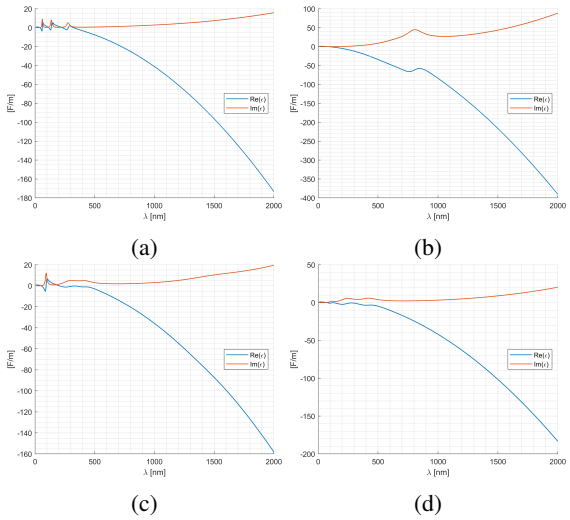

Fig. 1: Complex Dielectric Function: (a) Silver; (b) Aluminium; (c) Gold; (d) Copper.

In figure 1, it is evident the analyzed metals permittivity real part, $\mathfrak{Re}(\varepsilon)$, is predominantly negative and decreases for the longer wavelengths. This property is essential for the emergence of SPPs and their subsequent propagation.

B. Surface Plasmon Polaritons

A plasmon oscillation can be defined as the joint movement of conduction band electrons relative to fixed positive ions in a metal that is subjected to the incident light electric field [5]. These oscillations are propagating waves with a distinct frequency and wave vector. When these types of oscillations are present at the interface between a conductor and a dielectric, i.e., a dielectric-metal interface, they are labeled Surface Plasmons [2], [6]. Surface plasmons can couple the light in the form of a surface wave originating Surface Plasmon Polaritons. The SPPs are surface electromagnetic waves that propagate along the dielectric-metal interface plane. As a result, the fields are strongly confined between the metal and the dielectric.

In order for SPPs to take place, a few conditions must be met, the metal must present electric permittivity with negative real part, at the incident light frequency. As well as, the wave vector component of the incident light that is parallel to the dielectric-metal interface must be matched with the wave number of the SPP. For optical frequencies, few metal can satisfy the first condition, for instance gold, silver, platinum and aluminium. Additionally, due to boundary conditions imposed by Maxwell's equations, the SPP cannot be excited by TE waves, it can only be excited by TM waves [2].

As previously mentioned, an SPP can only be excited by a TM-polarized wave. One says the light is Transverse Magnetic polarized when the magnetic field is perpendicular to the plane of incidence. In isotropic materials, such as metal, the electric field is perpendicular to the magnetic field for TM waves.

In figure 2, an incident TM wave is portrayed at a dielectric-metal interface. Where the first medium is a dielectric with complex permittivity $\overline{\varepsilon}_d$, and the second medium is a metal with complex permittivity $\overline{\varepsilon}_m$. Both mediums are presumed to extend throughout the z-axis and are non-magnetic. The incident TM wave wave-vector is expressed by $\overline{\boldsymbol{k}} = [\overline{k}_x, 0, \overline{k}_z]$, while the electromagnetic field follows equation 4, in which ω is the incident light angular frequency, and p is d or m for dielectric or metal, respectively.

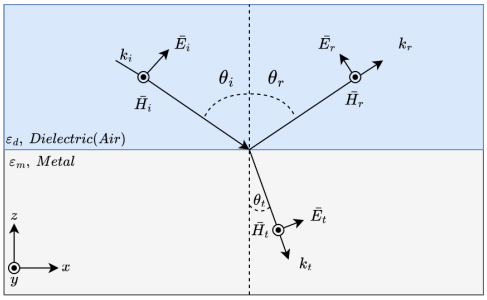

Fig. 2: Propagation of a TM wave in a dielectric-metal interface.

$$\begin{cases} \overline{E}_{x,p}(x,y,z,t) = E_0 e^{j\left(\overline{k}_x x + \overline{k}_{z,p}|z| - \omega t\right)} \\ \overline{E}_{z,p}(x,y,z,t) = \pm\frac{\overline{k}_x}{\overline{k}_{z,p}} E_0 e^{j\left(\overline{k}_x x + \overline{k}_{z,p}|z| - \omega t\right)} \\ \overline{H}_{y,p}(x,y,z,t) = H_0 e^{j\left(\overline{k}_x x + \overline{k}_{z,p}|z| - \omega t\right)} \end{cases} \tag{4}$$

Due to the lack of surface charges, the boundary conditions imply that the tangential components of the electromagnetic field should be continuous along the interface, resulting in the following conditions $\overline{E}_{x,d} = \overline{E}_{x,m}$ and $\overline{H}_{y,d} = \overline{H}_{y,m}$.

In that case, it is possible to extrapolate from Maxwell's equations the deduction present in equation 5 and equation 6, which in turn allows obtaining the SPP dispersion relation, i.e, $\mathfrak{Re}(\overline{k}_x)$, where k_0 is the incident wave-vector expressed trough $k_0 = \omega/c_0$, for which c_0 is the light speed in the vacuum. Additionally, a perpendicular wavevector component $\overline{k}_{z,p} = \left(\overline{\varepsilon}_p k_0^2 - \overline{k}_x^2\right)^{\frac{1}{2}}$, which will not be taken into account.

$$\nabla \times \overline{H} = \overline{\varepsilon}\frac{\partial \overline{E}}{\partial t} \Rightarrow \begin{cases} \frac{E_0}{H_0} = -\frac{\overline{k}_{z,m} c_0}{\overline{\varepsilon}_m \omega} \\ \frac{E_0}{H_0} = \frac{\overline{k}_{z,d} c_0}{\overline{\varepsilon}_d \omega} \\ \overline{k}^2 = \overline{k}_x^2 + \overline{k}_z^2 \end{cases} \Rightarrow \begin{cases} \frac{\overline{k}_{z,m} c_0}{\overline{\varepsilon}_m \omega} + \frac{\overline{k}_{z,d} c_0}{\overline{\varepsilon}_d \omega} \\ \overline{k}_x^2 + \overline{k}_{z,p}^2 = \overline{\varepsilon}_p \left(\frac{\omega}{c_0}\right)^2 \end{cases} \tag{5}$$

$$\overline{k}_x = k_0 \sqrt{\frac{\overline{\varepsilon}_m(\omega)\overline{\varepsilon}_d(\omega)}{\overline{\varepsilon}_m(\omega) + \overline{\varepsilon}_d(\omega)}} \tag{6}$$

The SPP dispersion relation curves allow us to identify resonance frequencies that appear when the SPP dispersion curve is on the right of the light curve, given by $\omega = c_0 \mathfrak{Re}(\overline{k}_x)/n\sqrt{\overline{\varepsilon}_d(\omega)}$, n being the dielectric refractive index. In this case, the dielectric medium is air, and it is assumed that $\overline{\varepsilon}_d = 1$(real and with no losses). Since SPPs propagate when the dispersion curve is on the right of the light curve, they present a smaller wavelength than the radiation in free space, therefore presenting an evanescent decay, implying that the fields exponentially decay away from the surface. The SPPs dispersion curves are obtained through the application of equation 6 for the metals previously described by the Drude-Lorentz model, yielding the curves present in figure 3 for the real part of the wavevector, where the black dashed line represents the light curve, and the curves present in figure 4 for the imaginary part of the wavevector.

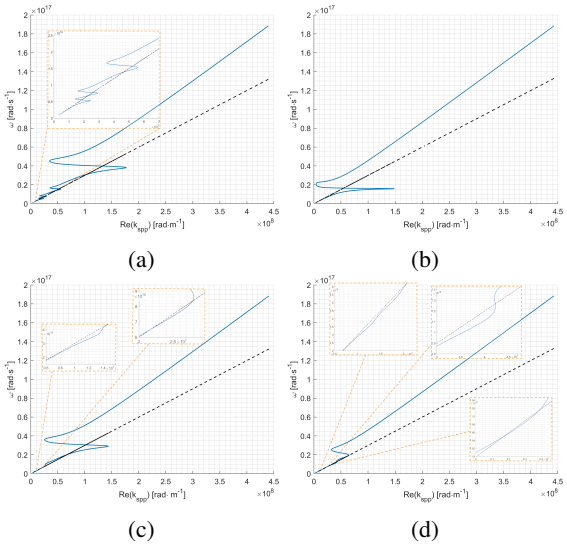

Fig. 3: Real SPP dispersion relation curves: (a) Silver; (b) Aluminium; (c) Gold; (d) Copper.

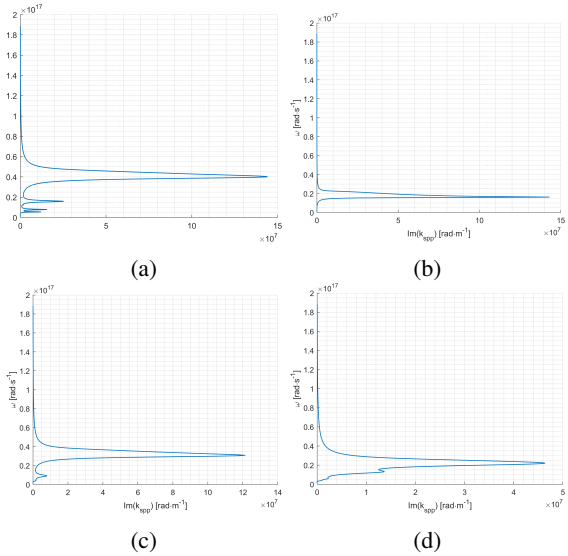

Fig. 4: Imaginary SPP dispersion relation curves: (a) Silver; (b) Aluminium; (c) Gold; (d) Copper.

For $\mathfrak{Re}(\overline{\varepsilon}_m) > 0$ the x and z components of the wavector are purely real, therefore resulting in radiative or unbound modes. This happens to the left of the light curve for angular frequencies higher than the plasma frequency, $\omega > \omega_p$.

On the other hand, when the metal's dielectric permittivity is between minus the dielectric's permittivity and zero, $-\varepsilon_d < \mathfrak{Re}(\overline{\varepsilon}_m) < 0$, the imaginary par of $\overline{k}_x$ is far greater than the real part, $\mathfrak{Im}(\overline{k}_x) \gg \mathfrak{Re}(\overline{k}_x)$, leading to quasi-bound propagation modes. In terms of angular frequency these modes take place for frequencies between $\frac{\omega_p}{\sqrt{1+\varepsilon_d}}$ and ω_p, meaning $\frac{\omega_p}{\sqrt{1+\varepsilon_d}} < \omega < \omega_p$. The fact that $\mathfrak{Im}(\overline{k}_x)$ exhibits high values grants the waves an evanescent decay. These waves decay exponentially with distance from the interface at which they are formed, the dielectric-metal interface.

Lastly, at metal's permittivity values bellow minus the dielectric's permittivity, $\mathfrak{Re}(\overline{\varepsilon}_m) < -\varepsilon_d >$, $\overline{k}_x$ is mostly real while $\overline{k}_z$ is predominantly imaginary resulting in bound modes of propagation. This behaviour takes place at frequencies bellow $\frac{\omega_p}{\sqrt{1+\varepsilon_d}}$, for $\omega < \frac{\omega_p}{\sqrt{1+\varepsilon_d}}$.

Resonance frequencies located in the range of radiative or bound modes, the metal transmission is very high, behaving like a transparent material. The real part of the wave-vector $\overline{k}_x$ approaches asymptotically the limit that separates quasi-bound from bound modes, which is given by $\frac{\omega_p}{\sqrt{1+\varepsilon_d}}$.

Through analysis of figure 3 it is attainable the resonance wavelengths for the several air-metal interfaces for the studied metals, by retrieving the frequencies corresponding to peak values of $\mathfrak{Re}(\overline{k}_x)$ to the right of the light curve. In table II, the mentioned resonance wavelengths are illustrated.

Silver presents four resonance wavelengths, three in the UV at 49, 123, and 249 nm and one in the Visible spectra at 355 nm. On the other hand, for Aluminium, there is a single resonance wavelength in the UV spectra at 119 nm. For gold, there are three resonance frequencies, two of which are in the

UV, at 64 and 238 nm, and one in the Visible at 536 nm. Lastly, Copper presents four resonance wavelengths, two in the UV at 100 and 158 nm, and two in the Visible at 360 and 526 nm.

TABLE II: Obtained resonance wavelengths.

	Aluminum	Gold	Silver	Copper
λ nm	119	64 238 536	49 123 249 355	100 158 360 526

III. Developed Model

A. Physics and Models

COMSOL Multiphysics is a Finite Element Analysis software, a numerical method used in mathematics and engineering to determine approximate solutions for differential equations. The software *COMSOL Multiphysics* allows for several types of physics interfaces. The physics interfaces employed are the Radio Frequency interfaces which compute the electric and magnetic fields in high-frequency systems. This interface possesses other subinterfaces, such as the Electromagnetic Waves, Frequency Domain interface that solves for time-harmonic electromagnetic field distributions. A Frequency Domain type of study is applied for source driven simulations for a single frequency or a sequence of frequencies.

Consequently, this physics interface solves the time-harmonic wave equation for the electric field described by equation 7, which presents solutions in the form of equation 8.

$$\nabla \times (\nabla \times \boldsymbol{E}) - k_0^2 \varepsilon_r \boldsymbol{E} = 0 \tag{7}$$

$$\boldsymbol{E}(x, y, z) = \overline{\boldsymbol{E}}(x, y)\, e^{-ik_z z} \tag{8}$$

The materials' models used are included in the COMSOL software. For metals, the 1998 Rakic fitting is used, which is found under the Inorganic Materials in the Optical section of the Materials. Therefore, the metals' permittivity follow the curves already studied in figure 1. The employed dielectric is air which is characterized by a constant, and real permittivity equal to unity. Lastly, the semiconductor chosen is Silicon (Si), which is characterized by the Aspnes and Studna fitting from 1983.

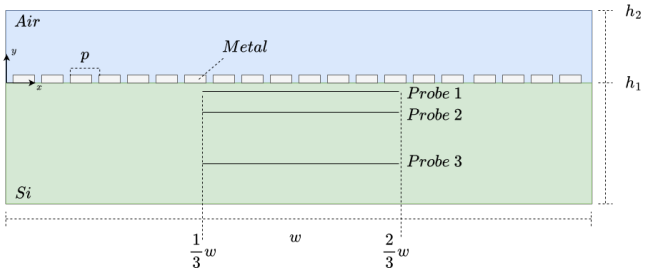

Fig. 5: Illustrative representation of the model.

In terms of structure, the design follows the representation in figure 5, where the width of the structure, w, is 9.05 μm. The design is composed by a dielectric layer (air), where an array of metal nanoantennas is contained, and a semiconductor layer. The developed model is bidimensional (2D) in order to reduce computation time. This approximation represents a transversal cut of a tridimensional structure, and this may be valid due to the fact that the transversal section is representative of the tridimensional device. Any two transversal planes drawn will be the same. The semiconductor layer has a height, h_1, of 2.2 μm, and the dielectric layer has a height, h_2, of $\frac{1}{3}h_1$. The metal nanoantenna's height depends on the geometry in analysis since different geometries are studied. However, the period, p, remains constant with a value of 450 nm. Similarly, the number of elements in the array is constant at 20 elements.

Additionally, the coordinate plane origin defined as the dielectric-metal interface left corner. This implies that for y higher than zero, it is in the dielectric medium, and for y bellow zero, it is in the semiconductor medium.

In the Frequency Domain study, it is necessary to define several Scattering Boundary Conditions. The initial values of the electric field are all set to zero. The incident electric field originates at $y = h_2$ and only has the x component different from zero, with an amplitude of 1 V/m.

1) Scattering Boundary Conditions: The Scattering Boundary Condition defines a boundary transparent for a scattered wave. The boundary is only perfectly transparent for scattered (outgoing) waves of the selected type at normal incidence to the boundary. That is, a plane wave at oblique incidence is partially reflected and so is a cylindrical wave or spherical wave unless the wavefronts are parallel to the boundary. That is, at the boundary the wave is decomposed into two components, perpendicular and parallel. The perpendicular component is absorbed at the boundary. Meanwhile, the parallel component keeps propagating. This condition is applied for $x = 0$, $x = w$, and $y = -h_1$ giving rise to well-defined boundaries.

2) Probe Placement: A crucial step in the model design is the definition of three probes present in figure 5. The distance from the dielectric-semiconductor interface is defined following the radiation zones for near-field and far-field, where each probe corresponds to the limit of the zones. Hence, the minimum wavelength considered for the delimitation of the radiation zones was 200 nm, even though some of the studies include shorter wavelengths that would yield distances too close to the interface for the overall range of frequencies studied. Moreover, the maximum wavelength studied is 700 nm, the upper limit of the visible spectrum. Consequently, at $d_1 = -\frac{200}{2\pi}$ nm is defined probe 1, at $d_2 = -200$ nm is located probe 2, and lastly, probe 3 is at $d_3 = -1500$ nm, since it is larger than twice 700 nm. As for the length of the probes, they are all $\frac{1}{3}w$ long, spanning from 3 μm to 6μm, in order to avoid the waves that might be reflected from the boundaries previously defined. That is, if the probe spanned throughout the entire semiconductor layer, from boundary to boundary, the electric field maxima would've probably been in the boundary points due to the interaction between the reflected waves at

the boundary.

3) Frequency Ranges: As formerly mentioned, the Frequency Domain study is applied to the simulation for a sequence of frequencies. The frequency ranges were all obtained similarly. Furthermore, the Visible Spectrum ranges from 400 nm to 700nm, noting with special importance that the Sun's radiation peak intensity is at a wavelength of approximately 500 nm. Consequently, a linearly spaced vector starting from 200 nm to 700 nm, with a spacing of 50 nm is created as a start. To this vector are then added the metal resonances obtained in table II, depending on which metal is present in the structure. The resulting vector is then converted to THz and the simulation frequency ranges are defined.

4) Nanoantenna Geometry: The study focuses on three aperture metal nanoantenna geometries rectangular, circular and triangular. In the rectangular geometry, the simulations are conducted for a metal thickness of 20 nm, present in figure 6a, and 50 nm, as seen in figure 6b, with a width of 400 nm. On the other hand, in the circular geometry, the circle is tangent to the dielectric-semiconductor interface, and it was tested for a radius of 100 nm (figure 6c) and 200 nm (figure 6d). Lastly, the triangular geometry, where the array consists of two triangles with base b side by side, with a base of 100 nm and 200 nm, as illustrated in figures 6e and 6f, respectively.

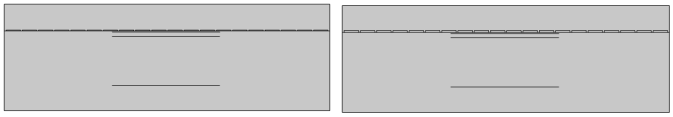

(a) Rectangular structure with 20 nm thickness.

(b) Rectangular structure with 50 nm thickness.

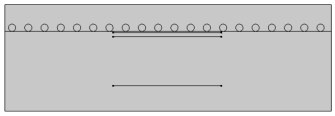

(c) Circular structure with 100 nm radius.

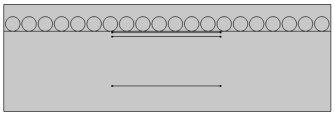

(d) Circular structure with 200 nm radius.

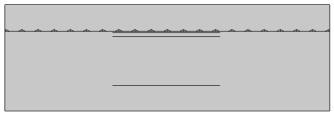

(e) Triangular structure with 100 nm base and 50 nm height.

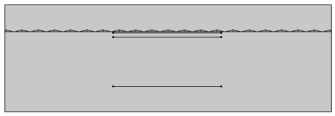

(f) Triangular structure with 200 nm base and 50 nm height.

Fig. 6: The different structure designs.

5) Mesh: The Mesh defines the discretization of the geometry, which divides the geometry into small units of simple shapes (mesh elements), allowing the computation of approximate solutions over each mesh element rather than the entire geometry. The type of mesh element is triangular, with a maximum element size of 6.767E-7 m, a minimum element size of 2.03E-8 m, and a maximum element growth rate of 1.5.

IV. Results Discussion

From the sections above, key findings emerge, for instance in table III, Silver achieves the greatest $|E_{max}|$ 7.22E-01 V/m at 550 nm for the rectangular structure of 50 nm thickness. Additionally, the highest $\int E$ obtained is 1.48E-06 for a circular structure with a 100 nm radius for a 700 nm wavelength. Overall, the Silver structures in tandem with the Silicon cell yield an electric field intensity greater than that of the Silicon cell alone 24 times.

The table IV contains the results for Aluminium. The highest $|E_{max}|$ achieved is 7.95E-01 V/m for the rectangular structure of 50 nm thickness at 500 nm. Also, it reaches its largest $\int E$ value, 1.43E-06, for the circular structure with a 100 nm radius for 700 nm wavelength. Combining the results for all the Aluminium antennas, the Silicon cell electric field intensity is surpassed a total of 21 times for this metal.

Concerning table V which illustrates the results for Gold, the antenna design that yields the greatest $|E_{max}|$ and $\int E$ the circular antenna with a 100 nm radius at 700 nm with an electric field of 6.17E-01 V/m and an $\int E$ of 1.42E-06 at 700 nm. Now, compiling the results for the gold antenna structures the electric intensity is greater than the Silicon cell peak field intensity a total of 19 times.

Lastly, the antenna design giving rise to the highest values for Copper, consulting table VI, is the circular antenna with a 100 nm radius at 700 nm with an electric field of 6.49E-01 V/m and an $\int E$ of 1.45E-06 at 700 nm. Analysing the table results one can observe that the electric field intensity surpasses the $|E_{max}|^{Si}$ 20 times. It can be concluded that the highest field concentration is for Aluminum with a field value of 7.95E-01 V/m at 500 nm. As for the electric field integral the highest value is reached for the Silver circular antenna with 100 nm radius.

For the rectangular nanoantenna, a higher field concentration is obtained for the 50 nm thick metal due to the fact that the added thickness facilitates the reflection of the electric field in the sides of the nanoantenna. Thus, resulting in a higher concentration of the electric field in the slit area.

Now analyzing from a geometry standpoint, the 20 nm thick rectangular antenna has the best result when using Silver with an electric field of 4.13E-01 V/m at 550 nm, yet is not an improvement compared with $|E_{max}|^{Si}$. In contrast, the 50 nm thick rectangular antenna has field enhancement for all the metals simulated, reaching its highest electric field of 7.95E-01 for Aluminium at 500 nm.

The circular geometry shows the electric field maxima for the same metal for both studied radii and the same wavelength. That is, for Silver at 700 nm the maximum electric field reached is 6.77E-01 V/m and 5.78E-01 V/m for the 100 nm and 200 nm radius, respectively.

Finally, the triangular geometry delivers the electric field maxima for the different base lengths for the same metal, Aluminium, but at distinct wavelengths. With a base length of 100 nm, the peak field is 5.08E-01 V/m at 700nm. As for the 200 nm base, at 500 nm the maximum field achieved is 6.36E-01 V/m. Notably, in a similar way to the circular geometry, the triangular geometries simulated all provide improvements for all considered metals for at least one of the frequencies when

compared to $|E_{max}|^{Si}$. The two-metal rectangular geometry resulted in no improvements.

It should also be noted that the geometry and metal used for the antenna not only influenced the electric field and its integral but also influenced the wavelengths for which it occurs. For example, for the 100 nm radius circular antenna, the maximum electric field intensity and integral all occurred for the same wavelength, at 700 nm, independently of the nanoantenna's metal.

REFERENCES

[1] R. A. M. Lameirinhas, J. P. N. Torres, A. Baptista, and M. J. M. Martins, "A new method to analyse the role of surface plasmon polaritons on dielectric-metal interfaces," *IEEE Photonics Journal*, vol. 14, no. 4, pp. 1–9, 2022.

[2] R. D. F. R. Gomes, M. J. Martins, A. Baptista, and J. P. N. Torres, "Study of a nano optical antenna for intersatellite communications," *Optical and Quantum Electronics*, vol. 49, 4 2017.

[3] N. Sharma, A. Joy, A. K. Mishra, and R. K. Verma, "Fuchs sondheimer–drude lorentz model and drude model in the study of spr based optical sensors: A theoretical study," *Optics Communications*, vol. 357, pp. 120–126, 2015. [Online]. Available: https://www.sciencedirect.com/science/article/pii/S0030401815300857

[4] A. D. Rakić, A. B. Djurišić, J. M. Elazar, and M. L. Majewski, "Optical properties of metallic films for vertical-cavity optoelectronic devices," *Appl. Opt.*, vol. 37, no. 22, pp. 5271–5283, Aug 1998. [Online]. Available: https://opg.optica.org/ao/abstract.cfm?URI=ao-37-22-5271

[5] R. Singh and A. K. Azad, "9 resonant field enhancement of terahertz waves in subwavelength plasmonic structures," 2013.

[6] I. Caetano, J. P. Torres, and R. Lameirinhas, "Simulation of solar cells with integration of optical nanoantennas," *Nanomaterials*, 10 2021.

TABLE III: Summary table of the results obtained for the Silver nanostructures - Probe 1.

		Rectangle thickness = 20 nm		Rectangle thickness = 50 nm		Circle r100		Circle r200		Triangle base = 100 nm		Triangle base = 200 nm	
	λ [nm]	$\lvert E_{max}\rvert$ [V/m]	$\int E$	$\lvert E_{max}\rvert$ [V/m]	$\int E$	$\lvert E_{max}\rvert$ [V/m]	$\int E$	$\lvert E_{max}\rvert$ [V/m]	$\int E$	$\lvert E_{max}\rvert$ [V/m]	$\int E$	$\lvert E_{max}\rvert$ [V/m]	$\int E$
UV	250	1.92E-02	4.86E-08	1.25E-02	2.18E-08	1.52E-02	3.18E-08	8.76E-04	1.10E-09	2.72E-02	6.13E-08	2.32E-02	4.38E-08
	300	1.70E-02	4.68E-08	1.46E-02	3.35E-08	1.78E-02	3.27E-08	2.82E-03	6.02E-09	1.76E-02	4.78E-08	1.65E-02	4.34E-08
	350	4.39E-02	1.28E-07	2.79E-02	7.69E-08	3.16E-02	5.10E-08	4.57E-04	7.40E-10	5.63E-02	1.37E-07	4.28E-02	1.17E-07
Visible Light	400	2.64E-01	6.35E-07	1.34E-01	3.05E-07	1.91E-01	4.93E-07	1.32E-01	3.23E-07	2.86E-01	6.71E-07	2.08E-01	5.53E-07
	450	3.47E-01	8.26E-07	4.68E-01	5.97E-07	2.67E-01	5.91E-07	1.09E-01	2.64E-07	3.77E-01	9.13E-07	2.85E-01	6.18E-07
	500	3.82E-01	8.97E-07	2.13E-01	4.38E-07	4.29E-01	9.65E-07	3.74E-01	8.92E-07	4.24E-01	9.94E-07	**5.51E-01**	**8.86E-07**
	550	**4.13E-01**	9.25E-07	**7.22E-01**	**8.16E-07**	4.63E-01	1.08E-06	4.34E-01	9.81E-07	4.43E-01	1.04E-06	5.27E-01	8.70E-07
	600	4.01E-01	**9.29E-07**	7.09E-01	8.12E-07	5.02E-01	1.20E-06	5.09E-01	1.14E-06	4.53E-01	1.06E-06	5.18E-01	8.66E-07
	650	3.77E-01	9.08E-07	5.83E-01	6.50E-07	6.18E-01	1.41E-06	5.66E-01	1.37E-06	4.59E-01	1.07E-06	5.25E-01	8.64E-07
	700	3.59E-01	8.96E-07	4.58E-01	6.68E-07	**6.77E-01**	**1.48E-06**	**5.78E-01**	**1.40E-06**	**4.71E-01**	**1.09E-06**	5.08E-01	8.67E-07
Resonance wavelengths	49	3.80E-06	1.63E-12	2.32E-06	7.02E-13	5.39E-06	6.13E-12	8.13E-07	5.89E-13	4.28E-06	6.96E-12	4.06E-06	2.54E-12
	123	3.47E-03	5.85E-09	1.85E-03	1.61E-09	7.08E-03	6.82E-09	6.21E-05	6.87E-11	6.51E-03	1.00E-08	4.93E-03	5.95E-09
	249	1.98E-02	5.02E-08	1.28E-02	2.27E-08	1.66E-02	3.31E-08	7.43E-04	9.14E-10	2.88E-02	6.20E-08	2.43E-02	4.54E-08
	355	4.40E-02	1.26E-07	2.69E-02	7.39E-08	3.38E-02	5.85E-08	1.19E-03	2.24E-09	5.65E-02	1.36E-07	4.27E-02	1.15E-07

TABLE IV: Summary table of the results obtained for the Aluminium nanostructures - Probe 1.

		Rectangle thickness = 20 nm		Rectangle thickness = 50 nm		Circle r100		Circle r200		Triangle base = 100 nm		Triangle base = 200 nm	
	λ [nm]	$\lvert E_{max}\rvert$ [V/m]	$\int E$	$\lvert E_{max}\rvert$ [V/m]	$\int E$	$\lvert E_{max}\rvert$ [V/m]	$\int E$	$\lvert E_{max}\rvert$ [V/m]	$\int E$	$\lvert E_{max}\rvert$ [V/m]	$\int E$	$\lvert E_{max}\rvert$ [V/m]	$\int E$
UV	250	2.55E-02	3.34E-08	8.54E-03	5.76E-09	2.95E-02	5.97E-08	2.44E-02	4.71E-08	5.07E-02	6.47E-08	2.11E-02	2.68E-08
	300	2.36E-02	2.45E-08	2.25E-02	1.28E-08	2.71E-02	4.05E-08	1.41E-02	3.42E-08	2.20E-02	3.78E-08	1.62E-02	1.93E-08
	350	5.86E-02	6.83E-08	7.09E-02	4.05E-08	6.37E-02	1.40E-07	4.49E-02	1.07E-07	5.98E-02	1.07E-07	4.86E-02	5.32E-08
Visible Light	400	2.84E-01	3.47E-07	2.87E-01	1.72E-07	3.41E-01	6.97E-07	1.88E-01	4.47E-07	3.02E-01	5.17E-07	2.06E-01	2.43E-07
	450	2.44E-01	3.95E-07	1.35E-01	1.14E-07	3.91E-01	8.28E-07	3.29E-01	7.64E-07	4.65E-01	8.01E-07	5.84E-01	5.31E-07
	500	**3.47E-01**	4.56E-07	**7.95E-01**	7.22E-07	4.85E-01	1.06E-06	3.73E-01	9.17E-07	4.72E-01	8.51E-07	**6.36E-01**	**5.78E-07**
	550	3.38E-01	4.89E-07	5.40E-01	6.44E-07	5.27E-01	1.20E-06	3.99E-01	1.07E-06	4.72E-01	8.68E-07	5.53E-01	5.55E-07
	600	3.31E-01	5.75E-07	4.47E-01	**7.74E-07**	5.43E-01	1.31E-06	**4.49E-01**	**1.20E-06**	5.05E-01	8.84E-07	5.11E-01	5.65E-07
	650	3.02E-01	**5.97E-07**	3.89E-01	7.42E-07	5.62E-01	1.38E-06	4.28E-01	1.16E-06	**5.08E-01**	8.84E-07	4.69E-01	5.63E-07
	700	3.18E-01	5.58E-07	3.80E-01	6.48E-07	**5.78E-01**	**1.43E-06**	3.90E-01	1.03E-06	4.91E-01	**9.14E-07**	4.21E-01	5.24E-07
Resonance wavelengths	119	2.58E-03	5.48E-09	3.48E-04	8.53E-10	8.35E-03	7.46E-09	4.51E-07	3.27E-13	5.35E-03	8.89E-09	4.05E-03	5.42E-09

TABLE V: Summary table of the results obtained for the Gold nanostructures - Probe 1.

		Rectangle, height 20 nm		Rectangle, height 50 nm		Circle, radius 100 nm		Circle, radius 200 nm		Triangle, base 100 nm		Triangle, base 200 nm	
	λ [nm]	$\lvert E_{max}$ [V/m]	$\int E$	$\lvert E_{max}$ [V/m]	$\int E$	$\lvert E_{max}$ [V/m]	$\int E$	$\lvert E_{max}$ [V/m]	$\int E$	$\lvert E_{max}$ [V/m]	$\int E$	$\lvert E_{max}$ [V/m]	$\int E$
UV	250	2.17E-02	4.33E-08	1.33E-02	1.72E-08	1.70E-02	3.80E-08	4.19E-03	6.47E-09	3.46E-02	6.12E-08	2.04E-02	3.76E-08
	300	1.81E-02	3.55E-08	1.39E-02	1.71E-08	1.94E-02	3.17E-08	3.59E-03	7.76E-09	1.93E-02	4.25E-08	1.57E-02	3.02E-08
	350	5.11E-02	1.15E-07	4.38E-02	6.40E-08	5.04E-02	1.05E-07	9.73E-03	2.29E-08	5.32E-02	1.29E-07	4.64E-02	9.93E-08
Visible Light	400	2.51E-01	5.85E-07	2.25E-01	3.52E-07	1.98E-01	4.86E-07	4.79E-02	1.24E-07	2.58E-01	6.45E-07	2.14E-01	5.08E-07
	450	3.10E-01	7.96E-07	2.65E-01	5.15E-07	1.97E-01	5.00E-07	4.68E-02	1.20E-07	3.51E-01	8.82E-07	2.75E-01	7.12E-07
	500	3.50E-01	9.10E-07	2.32E-01	5.59E-07	2.55E-01	6.89E-07	7.84E-02	2.12E-07	4.03E-01	1.00E-06	4.46E-01	8.77E-07
	550	3.91E-01	9.67E-07	3.39E-01	6.28E-07	3.73E-01	9.32E-07	2.12E-01	5.67E-07	4.26E-01	1.06E-06	4.74E-01	9.15E-07
	600	**4.00E-01**	**9.87E-07**	5.67E-01	**8.02E-07**	4.61E-01	1.12E-06	3.58E-01	8.59E-07	4.42E-01	1.08E-06	4.87E-01	**9.20E-07**
	650	3.99E-01	9.85E-07	**5.94E-01**	7.69E-07	5.21E-01	1.27E-06	4.62E-01	1.10E-06	4.50E-01	1.10E-06	**5.02E-01**	9.18E-07
	700	3.80E-01	9.67E-07	5.12E-01	6.96E-07	**6.17E-01**	**1.42E-06**	**5.46E-01**	**1.29E-06**	**4.58E-01**	**1.11E-06**	4.97E-01	9.17E-07
Resonance wavelengths	64	5.29E-05	2.93E-11	3.40E-05	1.50E-11	7.02E-05	1.03E-10	5.80E-06	7.13E-12	6.68E-05	1.14E-10	6.19E-05	4.05E-11
	238	2.36E-02	4.78E-08	1.58E-02	1.91E-08	2.15E-02	4.84E-08	4.32E-03	6.22E-09	3.40E-02	6.92E-08	2.65E-02	4.35E-08
	536	3.81E-01	9.54E-07	2.74E-01	5.87E-07	3.34E-01	8.65E-07	1.73E-01	4.62E-07	4.22E-01	1.04E-06	4.65E-01	9.06E-07

TABLE VI: Summary table of the results obtained for the Copper nanostructures - Probe 1.

		Rectangle thickness = 20 nm		Rectangle thickness = 50 nm		Circle r100		Circle r200		Triangle base = 100 nm		Triangle base = 200 nm	
	λ [nm]	$\lvert E_{max}\rvert$ [V/m]	$\int E$	$\lvert E_{max}\rvert$ [V/m]	$\int E$	$\lvert E_{max}\rvert$ [V/m]	$\int E$	$\lvert E_{max}\rvert$ [V/m]	$\int E$	$\lvert E_{max}\rvert$ [V/m]	$\int E$	$\lvert E_{max}\rvert$ [V/m]	$\int E$
UV	250	2.46E-02	4.03E-08	1.41E-02	1.49E-08	2.08E-02	4.13E-08	6.33E-03	1.06E-08	3.65E-02	6.02E-08	2.11E-02	3.41E-08
	300	1.80E-02	3.60E-08	1.34E-02	1.73E-08	1.91E-02	3.09E-08	3.33E-03	7.05E-09	1.93E-02	4.27E-08	1.55E-02	3.07E-08
	350	5.21E-02	1.08E-07	4.28E-02	5.45E-08	5.13E-02	1.07E-07	1.11E-02	2.70E-08	5.47E-02	1.26E-07	4.44E-02	9.10E-08
Visible Light	400	2.58E-01	5.40E-07	2.45E-01	2.98E-07	2.00E-01	5.20E-07	6.40E-02	1.79E-07	2.66E-01	6.16E-07	2.03E-01	4.45E-07
	450	3.07E-01	7.34E-07	2.66E-01	4.26E-07	2.03E-01	5.47E-07	6.69E-02	1.85E-07	3.63E-01	8.60E-07	2.67E-01	6.33E-07
	500	3.60E-01	8.58E-07	2.37E-01	4.76E-07	2.95E-01	7.95E-07	1.39E-01	3.73E-07	4.13E-01	9.78E-07	4.85E-01	8.32E-07
	550	**3.97E-01**	9.16E-07	4.63E-01	6.45E-07	4.04E-01	9.94E-07	2.64E-01	6.81E-07	4.32E-01	1.03E-06	4.93E-01	8.65E-07
	600	3.96E-01	**9.33E-07**	**6.09E-01**	**7.65E-07**	4.76E-01	1.16E-06	3.97E-01	9.42E-07	4.46E-01	1.06E-06	4.98E-01	8.72E-07
	650	3.87E-01	9.24E-07	5.72E-01	6.81E-07	5.48E-01	1.32E-06	4.90E-01	1.18E-06	4.54E-01	1.07E-06	**5.12E-01**	8.71E-07
	700	3.61E-01	8.99E-07	4.62E-01	6.05E-07	**6.49E-01**	**1.45E-06**	**5.45E-01**	**1.33E-06**	**4.66E-01**	**1.09E-06**	5.01E-01	**8.72E-07**
Resonance wavelengths	100	1.15E-03	9.58E-10	1.01E-03	5.07E-10	1.85E-03	2.75E-09	2.24E-04	2.86E-10	2.23E-03	3.08E-09	1.65E-03	1.27E-09
	158	9.41E-03	1.33E-08	7.84E-03	5.07E-09	1.44E-02	2.52E-08	1.83E-03	3.28E-09	2.11E-02	2.77E-08	1.40E-02	1.42E-08
	360	5.43E-02	1.11E-07	4.55E-02	5.64E-08	4.97E-02	1.10E-07	1.26E-02	3.21E-08	5.53E-02	1.31E-07	5.11E-02	9.70E-08
	526	3.82E-01	8.93E-07	3.31E-01	5.49E-07	3.50E-01	8.99E-07	2.00E-01	5.34E-07	4.27E-01	1.01E-06	4.81E-01	8.50E-07